Inorganic Chemistry

Article

pubs.acs.org/IC

Thermodynamic Study of CO_2 Sorption by Polymorphic Microporous MOFs with Open Zn(II) Coordination Sites

Spencer R. Ahrenholtz,[†] Carlos Landaverde-Alvarado,[‡] Macauley Whiting,[†] Shaoyang Lin,[†] Carla Slebodnick,[†] Eva Marand,[‡] and Amanda J. Morris*[,†]

[†]Department of Chemistry, Virginia Tech, Blacksburg, Virginia 24061, United States

[‡]Department of Chemical Engineering, Virginia Tech, Blacksburg, Virginia 24061, United States

Supporting Information

ABSTRACT: Two Zn-based metal organic frameworks have been prepared solvothermally, and their selectivity for CO_2 adsorption was investigated. In both frameworks, the inorganic structural building unit is composed of Zn(II) bridged by the 2-carboxylate or 5-carboxylate pendants of 2,5-pyridine dicarboxylate (pydc) to form a 1D zigzag chain. The zigzag chains are linked by the bridging 2,5-carboxylates across the Zn ions to form 3D networks with formulas of $Zn_4(pydc)_4(DMF)_2{\cdot}3DMF$ (**1**) and $Zn_2(pydc)_2(DEF)$ (**2**). The framework (**1**) contains coordinated DMF as well as DMF solvates (DMF = *N*,*N*-dimethylformamide), while (**2**) contains coordinated DEF (DEF = *N*,*N*-diethylformamide). (**1**) displays a reversible type-I sorption isotherm for CO_2 and N_2 with BET surface areas of 196 and 319 m^2/g, respectively. At low pressures, CO_2 and N_2 isotherms for (**2**) were not able to reach saturation, indicative of pore sizes too small for the gas molecules to penetrate. A solvent exchange to give (**2**)-**MeOH** allowed for increased CO_2 and N_2 adsorption onto the MOF surface with BET surface areas of 41 and 39 m^2/g, respectively. The binding of CO_2 into the framework of (**1**) was found to be exothermic with a zero coverage heat of adsorption, Q_{st}^0, of −27.7 kJ/mol. The Q_{st}^0 of (**2**) and (**2**)-**MeOH** were found to be −3 and −41 kJ/mol, respectively. The CO_2/N_2 selectivity for (**1**), calculated from the estimated K_H at 296 K, was found to be 42. At pressures relevant to postcombustion capture, the selectivity was 14. The thermodynamic data are consistent with a mechanism of adsorption that involves CO_2 binding to the unsaturated Zn(II) metal centers present in the crystal structures.

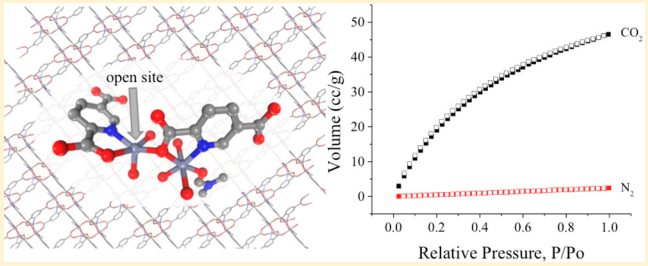

INTRODUCTION

Metal organic frameworks (MOFs) are synthetically tunable materials composed of metal or metal cluster nodes bound by multidentate organic linkers to form 3D crystalline structures with a network of interconnected pores.[1,2] The porous nature of MOFs allows for applications in areas such as gas storage and separation, heterogeneous catalysis, sensors, and drug delivery.[3−13] Specifically, porous materials show promise for applications in the separation of gas mixtures, such as O_2/N_2 for medical devices,[14] CO/H_2 for fuel cell applications,[15] N_2/H_2 for ammonia synthesis,[16] and CO_2/N_2 from combustion power plants.[7] An area of increased interest is the development of materials for CO_2 capture due to the rising levels of the greenhouse gas in the atmosphere. One of the main sources of increased atmospheric CO_2 is power plant emissions.[7,17] CO_2 sequestration can be applied precombustion or postcombustion, and the material properties for each process are unique. Precombustion capture occurs under high-pressure conditions (up to 70 bar) with high concentrations of CO_2 (40%). Therefore, materials with moderate to high surface areas are considered critical for these applications. Postcombustion capture, on the other hand, occurs near atmospheric pressure at low CO_2 concentration (15%), and therefore, the interactions between the adsorbent and CO_2 play a crucial role.

There are two main mechanisms for gas separation: kinetic separation and thermodynamic separation. For kinetic separation, which is based on the diffusivities of the gases into the pores, design of the MOF pores with respect to the kinetic diameter for each component is crucial.[18] However, *a priori* design of a 3D MOF structure is a difficult task despite recent advances with preformed secondary building units.[19] For thermodynamic separation, desired selectivity is the product of the affinity of the material toward each component.[18] With the composition of postcombustion flue gas being predominantly N_2 (~73−77%, kinetic diameter = 3.64 Å), followed by CO_2 (~15−16%, kinetic diameter = 3.30 Å), high selectivity of materials for CO_2 over N_2 is essential for postcombustion capture.[7,18,20] The small kinetic diameter of both N_2 and CO_2 requires the use of microporous materials to enable kinetic separation. However, it should be noted that the relatively similar kinetic diameters for N_2 and CO_2 preclude efficient separation from kinetic effects alone.

Many synthetic modifications to MOFs have been shown to increase the affinity of the material for CO_2 over N_2. These techniques often exploit the higher polarizability of CO_2 in

Received: January 5, 2015
Published: April 21, 2015

DOI: 10.1021/ic503047y
Inorg. Chem. 2015, 54, 4328−4336

comparison to symmetric N_2. For example, the slight positive charge that rests on the carbon of the CO_2 is susceptible to attack by Lewis bases. This is well-known in the carbon capture literature, as the formation of carbamates from the interaction between CO_2 and liquid amines is currently an industrial method for CO_2 sequestration.[21] The same functionality has been built into MOFs including Cu-BTTri-mmen,[22] CAU-1,[23] Bio-MOF-11,[24] and NH_2-Mil-53(Al),[25] resulting in impressive CO_2 storage capacities (15−24 wt % at 1 bar). Recently, a Zn-based MOF with multiple exposed Lewis basic sites on the linker displayed tremendous CO_2 sorption capacities. A high CO_2 uptake (36 wt % at 1 bar) was attributed to multipoint interactions between the CO_2 and the π-electrons and nitrogen atoms of the aromatic tetrazole ring as well as the alkane chains of the linker.[26] Another common approach is to include exposed cationic metal sites that can interact with the oxygen atoms of the CO_2. This is exemplified in the CPO-27-M (or M-MOF-74) series. Indeed, these materials exhibit extremely high CO_2 adsorption capacities of up to 27 wt % at 1 bar and 298 K.[27]

In this work, we report the solvothermal synthesis and characterization of two new microporous MOFs that have coordinatively unsaturated Zn(II) sites without the need for activation: $Zn_4(pydc)_4(DMF)_2{\cdot}3DMF$ (**1**) and $Zn_2(pydc)_2(DEF)$ (**2**), where pydc is 2,5-pyridine dicarboxylate, DMF is dimethylformamide, and DEF is diethylformamide. The CO_2 and N_2 gas sorption properties of these two materials are presented and compared to known MOF-69C, $Zn_3(OH)_2(bdc)_2{\cdot}2DEF$,[28] where bdc is 1,4-benzene dicarboxylate. The thermodynamic parameters, Q_{st} and Q_{st}^0, for the structures were calculated. The selectivity of (**1**), the most promising CO_2 adsorption material, was determined at pressures relevant to postcombustion CO_2 capture.

EXPERIMENTAL SECTION

Materials. The following reagents and solvents were purchased from the indicated commercial suppliers: zinc(II) nitrate hexahydrate (Sigma-Aldrich, 98%); 2,5-pyridinedicarboxylic acid (Aldrich, 98%); 1,4-benzenedicarboxylic acid (Acros, 99%); *N*,*N*-dimethylformamide (DMF; Spectrum, spectrophotometric grade); *N*,*N*-diethylformamide (DEF; Acros, 99%); methanol (MeOH; Spectrum, HPLC grade); acetone (Spectrum, HPLC grade); and chloroform (Spectrum, HPLC grade). Samples were submitted to Galbraith Laboratories, Inc., for elemental analysis.

Synthesis of $Zn_4(pydc)_4(DMF)_2{\cdot}3DMF$ (1). In a 20 mL vial, $Zn(NO_3)_2{\cdot}6(H_2O)$ (250 mg, 0.840 mmol) was dissolved in 10 mL of DMF, followed by the addition of 2,5-pyridinedicarboxylic acid (144 mg, 0.862 mmol). The vial was capped and sonicated until turbid and heated to 100 °C for 2 days. A vial containing colorless prisms was removed from the oven while hot and allowed to cool to RT. The crystals were collected via vacuum filtration and rinsed with DMF (257 mg, 95% yield based on $Zn(NO_3)_2{\cdot}6(H_2O)$). Anal. Calcd for $C_{43}H_{47}N_9O_{21}Zn_4$ (**1**): C, 40.12%; H, 3.68%, N, 9.79%; Zn, 20.31%. Found: C, 40.47%; H, 3.85%, N, 9.59%; Zn, 20.0%.

Synthesis of $Zn_2(pydc)_2(DEF)$ (2). In a 20 mL vial, $Zn(NO_3)_2{\cdot}6(H_2O)$ (177 mg, 0.596 mmol) was dissolved in DEF (4.883 mL). To the vial, 2,5-pyridinedicarboxylic acid (33 mg, 0.197 mmol) was added along with deionized water (0.177 mL). The vial was capped and sonicated until clear and heated to 75 °C for 3 days. A vial containing colorless parallelepipeds was removed from the oven while hot and allowed to cool to RT. The crystals were collected via vacuum filtration and rinsed with DEF (51.6 mg, 94% yield based on pydc). Anal. Calcd for $C_{19}H_{17}N_3O_9Zn_2$ (**2**): C, 40.67%; H, 3.05%; N, 7.49%; Zn, 23.31%. Found: C, 39.93%; H, 3.12%; N, 7.48%; Zn, 22.2%.

Synthesis of MOF-69C: $Zn_3(OH)_2(bdc)_2{\cdot}2DEF$. MOF-69C was prepared according to a previously published procedure.[28]

Single-Crystal X-ray Diffraction. Data sets were collected on an Agilent Gemini E Ultra diffractometer operating with MoKα radiation. The data collection routine, unit cell refinement, and data processing were carried out with the program CrysAlisPro.[29] The structure was solved using SHELXS-97[30] and refined using SHELXL-97[30] via OLEX2.[31] Figures were generated with OLEX2[31] or Mercury.[32] Void spaces were calculated using OLEX2 v1.2.6 with resolution = 0.2/Å; distance = 0.0/Å, probe = 1.2/Å, and grid = 0.7/Å.[31]

Structure of (1). The Laue symmetry and systematic absences were consistent with the monoclinic space group $P2_1/n$. The structure is a 3D-framework with solvent channels containing 1.5 DMF/asymmetric units. One DMF is located on a general position and modeled with 2-position disorder with relative occupancies that refined to 0.701(10) and 0.299(10). The minor conformation was modeled isotropically. The second DMF is disordered across an inversion center and constrained to 1/2-occupancy for each conformation. A PART −1 and FRAG/FEND commands were used to model the DMF, and an isotropic model was used. The final refinement model involved anisotropic displacement parameters for all non-hydrogen atoms of the framework and the major conformation of the DMF. A riding model was used for all hydrogen atoms.

Structure of (2). The Laue symmetry and systematic absences were consistent with the orthorhombic space group *Pbca*. A 2-position disorder model was used for the DEF, with relative occupancies that refined to 0.889(10) and 0.111(10). The final refinement model involved anisotropic displacement parameters for non-hydrogen atoms and a riding model for all hydrogen atoms. A SIMU command was used to restrain the ADPs in the disordered region of the DEF.

Powder X-ray Diffraction (PXRD). PXRD experiments were carried out on a Rigaku MiniFlex 600 with Cu(Kα) radiation (Cu−Kα = 1.5418 Å). The PXRD measurements were carried out over a 2θ range of 3−60° in continuous scanning mode (1.0°/min) and a resolution of 0.1°. The powder patterns of the materials were simulated in Mercury[32] and compared to the experimental patterns for structural confirmation and sample purity. PXRD was also used to monitor the stability of the frameworks with temperature. Prepared samples of (**1**), (**2**), and MOF-69C were each held at the desired temperature under vacuum for 1 h, followed by the immediate collection of a room temperature PXRD pattern. The same samples were then heated to the next temperature, and the same procedure was followed.

Attenuated Total Reflectance Fourier-Transform Infrared Spectroscopy (ATR-FTIR). ATR-FTIR spectra were obtained on a Varian 670 FT-IR Spectrometer equipped with a diamond Specac Golden Gate attachment. All spectra are an average of 24 scans for powder samples and were recorded from 4000 to 400 cm^{-1} with 4 cm^{-1} resolution. A background spectrum collected on air was subtracted from sample spectra. The spectra were not corrected for the depth of wavelength penetration.

Thermogravimetric Analysis (TGA). A Q-series TGA from TA Instruments was used to analyze thermal stability. A ∼10 mg sample was placed on an aluminum pan and heated at a rate of 10 °C/min under nitrogen over the temperature range of 25−600 °C.

Solvent Exchange. To allow for exchange with the solvents of crystallization within the MOFs, the as-synthesized materials were immersed in a more volatile solvent (e.g., methanol, acetone, chloroform). The solvent was decanted and replaced with fresh solvent 3 times over the course of 48 h. The resulting exchanged MOF crystallites were collected via vacuum filtration and allowed to dry in air.

Gas Sorption Isotherms. The sorption isotherm measurements were collected on a Quantachrome Autosorb-1. The samples were synthesized according to the procedures above and placed in a 6 mm large bulb sample cell, which was degassed under vacuum for 24 h with a temperature of 90 °C for the first 5 h and no temperature for the remaining time. The surface areas of the materials were determined by fitting the adsorption data within the 0.05−0.3 P/P_0 pressure range to the BET[33] and Langmuir[34] equations,[35] and the total pore volume was determined by a single point method taken at P/P_0 = 0.99. The pore size distribution was determined by applying the nonlocal density

DOI: 10.1021/ic503047y
Inorg. Chem. 2015, 54, 4328−4336

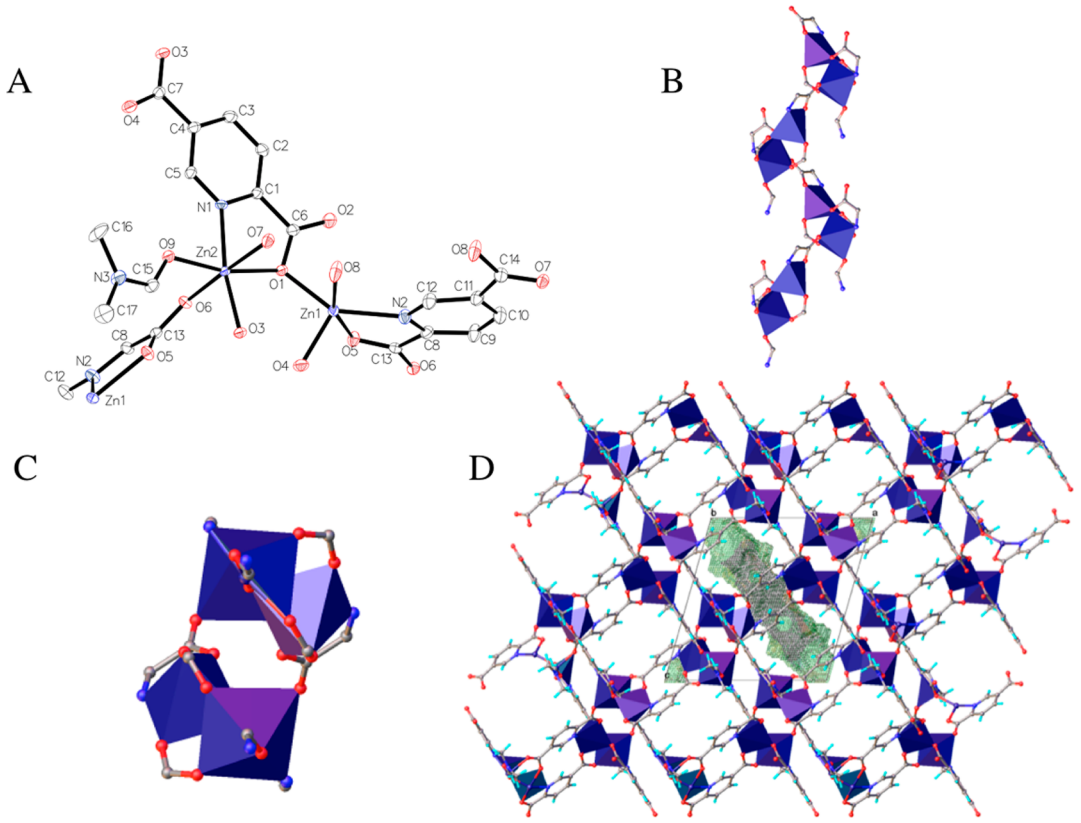

Figure 1. (A) Anisotropic ellipsoid drawing (50% probability) of (**1**) depicting the Zn dimer. H atoms and DMF solvate are omitted for clarity. (B) The 1D zigzag chains as viewed down the *a* axis. (C) The 1D zigzag chains as viewed down the *b* axis. (D) The packing diagram, as viewed down the *b* axis, depicting the pydc linking of the 1D chains along the [101] and [10$\bar{1}$] crystallographic directions. The wireframe depicts the void space when all DMF solvate is removed.

Table 1. Crystal Data and Structure Refinement for MOFs (1) and (2)

	(**1**)	(**2**)
identification code	$Zn_4(pydc)_4(DMF)_2{\cdot}3DMF$	$Zn_2(pydc)_2(DEF)$
chemical formula	$C_{43}H_{47}N_9O_{21}Zn_4$	$C_{19}H_{17}N_3O_9Zn_2$
formula mass	1287.38	561.09
crystal system	monoclinic	orthorhombic
space group	$P2_1/n$ (No. 14)	*Pbca* (No. 61)
wavelength/Å	0.71073	0.71073
a/Å	14.0003(3)	12.23325(19)
b/Å	12.1692(2)	17.4883(3)
c/Å	14.6711(3)	20.3322(5)
α/deg	90.00	90.00
β/deg	105.867(2)	90.00
γ/deg	90.00	90.00
unit cell volume/Å^3	2404.33(8)	4349.85(14)
Z	2	8
μ/mm^{-1}	2.065	2.262
density/g cm^{-3}	1.778	1.714
T/K	100	100
2θ range/deg	3.46−32.33	3.53−30.52
data measured	8062 [*R*(int) = 0.0607]	6633
unique data	5913	5162
goodness of fit	1.040	1.110
R indices [$I > 2\sigma(I)$][a,b]	R1 = 0.0468	R1 = 0.0492
	wR2 = 0.1008	wR2 = 0.1036
R indices (all data)[a,b]	R1 = 0.0762	R1 = 0.0677
	wR2 = 0.1150	wR2 = 0.1112

[a] $R1 = \sum||F_o| - |F_c||/\sum|F_o|$. [b] $wR = (\sum[w(F_o^2 - F_c^2)^2]/\sum|w(F_o^2)^2|)^{1/2}$, where $w = 1/[\sigma^2(F_o)^2 + (aP)^2 + bP]$, $P = [(F_o)^2 + 2(F_c)^2]/3$.

DOI: 10.1021/ic503047y
Inorg. Chem. 2015, 54, 4328−4336

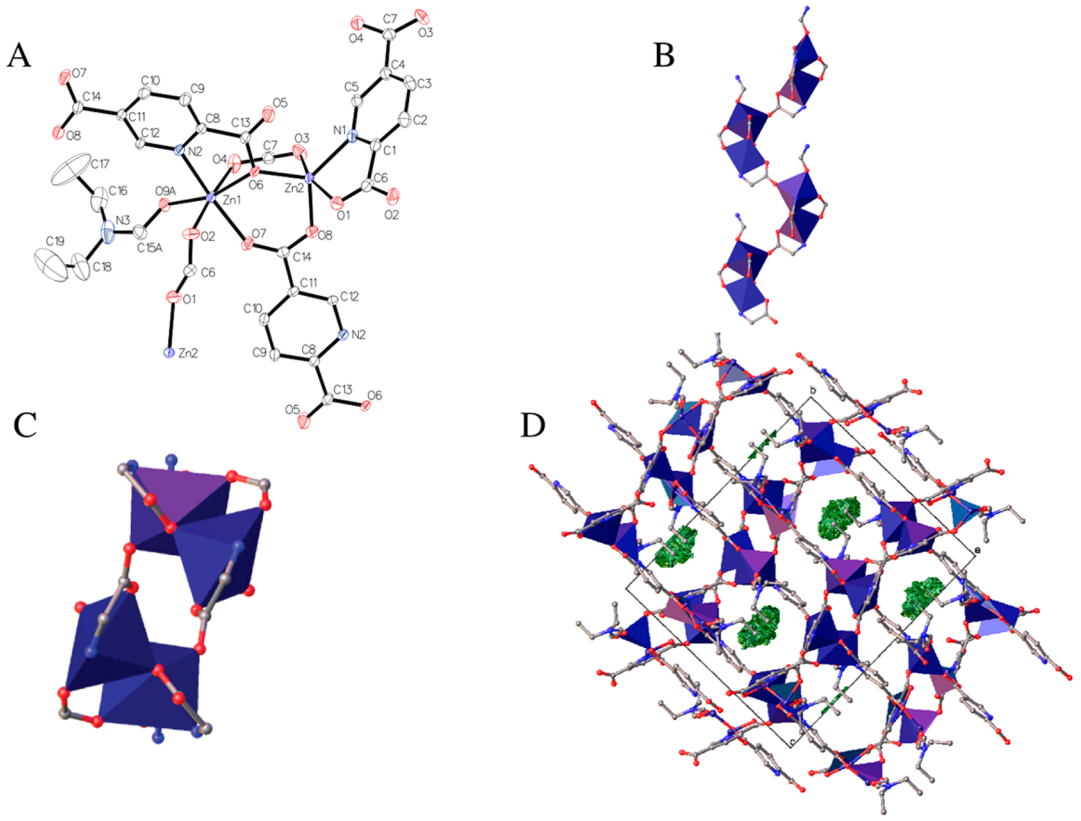

Figure 2. (A) Anisotropic ellipsoid drawing (50% probability) of (**2**) depicting the Zn dimer. H atoms and the minor conformation of the disordered DEF are omitted for clarity. (B) The 1D zigzag chains as viewed down the *b* axis. (C) The 1D zigzag chains as viewed down the *a* axis. (D) The packing diagram, as viewed down the *a* axis, depicting the pydc linking of the 1D chains along the [010] and [001] crystallographic directions. The wireframe depicts the void spaces.

functional theory (NLDFT) method on a slit pore equilibrium model to the CO_2 isotherm data at 273 K using the Autosorb software.

RESULTS AND DISCUSSION

Synthesis and Characterization. *Structure of $Zn_4(pydc)_4(DMF)_2{\cdot}3DMF$ (**1**).* The asymmetric unit of (**1**) contains 2 unique Zn atoms, 2 pydc ligands, 1 metal-coordinated DMF, and 1.5 DMF solvates. The pydc plays two roles in the formation of the 3D MOF. First, pydc bridges the Zn atoms by a single carboxylate in a $\kappa O^5{:}O^{5'}$ fashion, a $\kappa N^1,O^2{:}O^2$, or a $\kappa O^2{:}O^{2'}$ fashion to form 1D chains of secondary building units. Second, pydc bridges Zn atoms across the aromatic ring via the 2- and 5-carboxylates. Overall, the two pydc ligands in the asymmetric unit are each tetradentate with coordination μ_4-($\kappa^5N^1,O^2{:}O^2{:}O^5{:}O^{5'}$) and μ_4-($\kappa^5N^1,O^2{:}O^{2'}{:}O^5{:}O^{5'}$).

The secondary building unit is composed of Zn dimers ($d_{Zn1\text{—}Zn2}$ = 3.464 Å) that are bridged by three different pydc ligands, one coordinated $\kappa N^1,O^2{:}O^2$ fashion, and two coordinated $\kappa O^5{:}O^{5'}$ (Figure 1A). Zn1 has a distorted square pyramidal geometry, with three coordination sites filled by O atoms from the 3 bridging carboxylates, and the fourth and fifth coordination sites filled by a bidentate pydc ($\kappa N^1,O^2$). Zn2 has a distorted octahedral geometry, with four coordination sites filled by a pyridyl nitrogen and 3 O atoms of the bridging pydc ligands, the fifth site is filled by a pydc O atom, and the sixth site is filled by the O atom of the DMF. The dimers are linked along the *b* axis by a pydc bridging in a $\kappa O^2{:}O^{2'}$ fashion to form 1D zigzag chains (Figure 1B,C). The Zn—Zn distance between neighboring Zn dimers is 5.356 Å. This unusual coordination has been reported previously.[36] In the earlier structure, however, the Zn dimers bridge in the same $\kappa O^2{:}O^2$ fashion, but cyclize to form isolated Zn_4 clusters instead of zigzag chains. The pydc organic linkers that connect the zigzag chains run parallel to the crystallographic [101] and [10$\bar{1}$] directions to form the 3D framework.

In addition to the coordinated DMFs, there are 3 DMF solvates, giving a formula unit of $Zn_4(pydc)_4(DMF)_2{\cdot}3DMF$ (corresponds to 1.5 DMF solvates/asymmetric unit; 6 DMF solvates/unit cell). TGA and PXRD demonstrate that the crystals maintain their structural integrity upon removal of one DMF/formula unit (*vide infra*). Removal of a single DMF gives a void of 79.5 Å^3/formula unit (i.e., 2 symmetry equivalent voids totaling 159.1 Å^3/unit cell). If all 3 DMF solvates/formula unit are removed, the void volume is 317 Å^3 (634 Å^3/unit cell) and the void space is no longer an isolated cavity but instead channels through which solvent and gases can permeate (Figure 1D). Although the crystal structure is not stable upon removal of all 3 DMF solvates/formula unit, PXRD does indicate that the material is still crystalline, even if the structure has changed. In addition, it is conceivable that removal of a single DMF gives the remaining DMFs enough mobility for gas permeation. The structural purity of the as-synthesized MOF was confirmed by comparison of the experimental PXRD pattern with the pattern calculated from single-crystal data (Figure S1, Supporting Information). The crystallographic information on (**1**) is summarized in Table 1 and Tables S1—S2 (Supporting Information).

*Structure of $Zn_2(pydc)_2(DEF)$ (**2**).* The asymmetric unit of (**2**) contains two unique Zn atoms, two pydc ligands, and one

DOI: 10.1021/ic503047y
Inorg. Chem. 2015, 54, 4328—4336

metal-coordinated DEF. The two unique Zn atoms have the exact same connectivity as in (**1**) (Figure 2A) to generate the same 1D zigzag chains (Figure 2B,C). The Zn−Zn distance in the dimer is 3.438 Å, and the closest distance between dimers is 5.782 Å. The pydc organic linkers that connect the zigzag chains run parallel to the crystallographic *a* and *b* axes to form the 3D framework. Unlike (**1**), structure (**2**) has no solvents of crystallization. The void volume/unit cell is 161.1 $Å^3$ and is composed of 8 symmetrically equivalent voids of 20.1 $Å^3$ each. Comparison of the experimental PXRD pattern with the pattern calculated from the single-crystal data confirmed the sample homogeneity (Figure S2, Supporting Information). The crystallographic information on (**2**) is summarized in Table 1 and Tables S3 and S4 (Supporting Information).

Structure of MOF-69C: $Zn_3(OH)_2(bdc)_2{\cdot}2DEF$. The structure of MOF-69C has been reported previously and consists of an extended 3D framework with infinite 1D chains of zinc oxyhydroxide bridged by the 1,4-benzenedicarboxylate ligand.[28,37] The structure of MOF-69C contains octahedrally and tetrahedrally coordinated Zn(II) metal centers. To confirm the synthesis and determine phase purity, experimental PXRD patterns were compared to the calculated powder pattern from the literature reported single-crystal data, and TGA was performed (Figures S3 and S4, Supporting Information).

Fourier-transform infrared spectroscopy (FTIR) was used to characterize the MOFs. The spectrum for the 2,5-pyridinedicarboxylic acid linker displays features corresponding to the C═O stretch of the carboxylic acids at 1720 cm^{-1} (Figure 3, red). The spectra of (**1**) and (**2**) demonstrate a shift in these peaks to lower wavenumbers (1608 and 1616 cm^{-1}, respectively) due to the chelation of the carboxylic oxygen atoms to the Zn metal in the MOF framework (Figure 3). Features due to the O-H stretch as well as the aromatic C-H stretch (3093 and 2844 cm^{-1}, respectively) are observed in the 2,5-pyridinedicarboxylic acid spectrum (Figure 3, red). The O-H stretch is not present in the spectra of (**1**) and (**2**) (Figure 3, black and blue), consistent with coordination of the oxygen to the metal atom of the MOF. The appearance of peaks at 1043 and 1039 cm^{-1} in the spectra for (**1**) and (**2**), respectively, is also indicative of an M−N bond.[38]

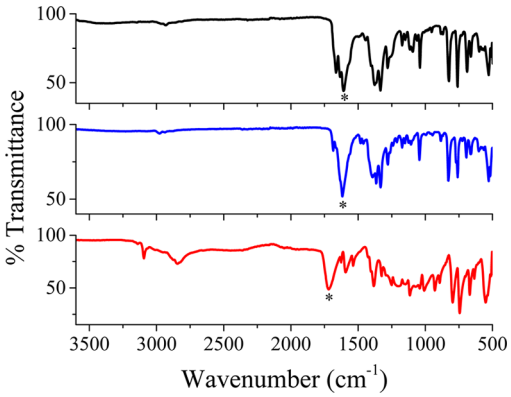

Figure 3. ATR-FTIR spectra with the designated (*) C═O stretches of the linker and the corresponding carboxylato stretches of the MOFs of (**1**) (black; 1608 cm^{-1}), (**2**) (blue; 1616 cm^{-1}), and 2,5-pyridine dicarboxylic acid (red; 1720 cm^{-1}). As the carboxylic oxygen becomes the carboxylato chelating functionality present in the MOF structures, there is a corresponding decrease in the frequency of this stretch.

The thermal stability and solvent loss of the MOFs were investigated using thermal gravimetric analysis (TGA). The TG curve of (**1**) reveals weight losses at 85 and 150 °C (obs: 6.38% and 10.5%, respectively; 16.88% total), consistent with the removal of 3 DMF solvates (calcd: 17.04%). A third loss at 270 °C (obs: 6.4%) is consistent with desorption of Zn-coordinated DMF (calcd: 5.68%). The removal of the second bound DMF occurs concomitantly with MOF degradation at ∼350 °C (Figure 4A). The TG curve of (**2**), with pore-contained solvate molecules, displays thermal stability up to 400 °C, where loss of bound DEF occurs concurrently with MOF degradation (Figure 4B). The TG curve of MOF-69C was consistent with previously reported results (Figure S4, Supporting Information).[37]

In addition to TGA, the effect of varied temperature on the structure was further investigated by PXRD after evacuation. Bulk crystalline samples were ground into powders and heated at the desired temperature under vacuum for 1 h, followed by immediate PXRD analysis at room temperature (Figure 5). The crystalline structure of (**1**) is stable upon removal of one DMF solvate (loss at 85 °C) but undergoes a structural rearrangement upon removal of a second DMF solvate (loss beginning at 150 °C) (Figure 5A). The crystal structure of (**2**) remains stable up to 260 °C, consistent with the TG curve (Figure 5B). MOF-69C undergoes a structural change between 130 and 196 °C, which is consistent with loss of a DEF solvate in the TG curve (Figure 5C). The removal of the second DEF molecule results in further change in the PXRD pattern at 230 °C. These results are consistent with the previously reported PXRD patterns for MOF-69C after removal of the DEF solvent at 200 °C.[39]

Gas Sorption Properties. Excess CO_2 gas sorption isotherms were measured for (**1**), (**2**), and MOF-69C at 273 K (Figure 6A,B; Figures S5−S7, Supporting Information). (**1**) displays the greatest affinity for CO_2 (58.946 mL/g at ∼1 atm) and exhibits a reversible type-I isotherm, consistent with a permanently microporous material.[35] The BET and Langmuir surface areas for (**1**) were calculated to be 196 and 390 m^2/g, respectively. The total pore volume was determined by the single point method to be 0.116 cm^3/g. DFT and Monte Carlo simulations determined a pore width of 7.17 Å, consistent with the crystal structure. The isotherms for (**2**) and MOF-69C display a lower affinity for CO_2 and did not reach a plateau within the pressure range observed, suggesting that the pore sizes of the frameworks are too small to reach equilibrium at the experimental pressure values (Figure 6; Figures S6 and S7, Supporting Information).

In order to increase the adsorptive properties of the MOFs, exchange with methanol was performed on (**1**) and (**2**). It can be observed that (**1**) undergoes a structural change after methanol is exchanged with DMF in the pores (Figures S8 and S9, Supporting Information). Even with exchange of DMF, the resulting surface area of (**1**) did not increase (Figure S10, Supporting Information). Not surprisingly, the structure of (**2**), which has no solvent of crystallization, was maintained after methanol exchange (Figure S11, Supporting Information). The TG curve of the exchanged material, (**2**)-**MeOH**, shows that methanol is present (Figure S12, Supporting Information). After evacuation of (**2**)-**MeOH** at 90 °C for 5 h, the TG curve recovers the as-synthesized temperature-dependent behavior (Figure S13, Supporting Information). The sorption properties of (**2**)-**MeOH** were studied with CO_2 at 273 K and display a type-1 reversible isotherm with a low CO_2 uptake of 12.7445

DOI: 10.1021/ic503047y
Inorg. Chem. 2015, 54, 4328−4336

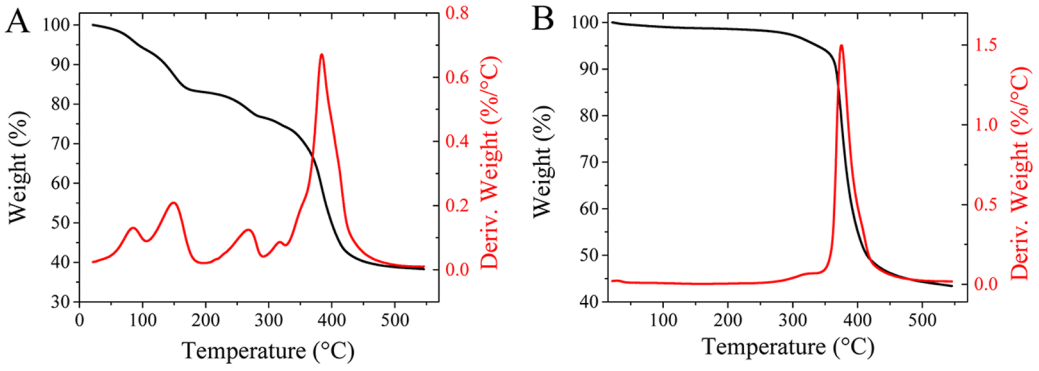

Figure 4. TG curves of (A) (**1**) and (B) (**2**).

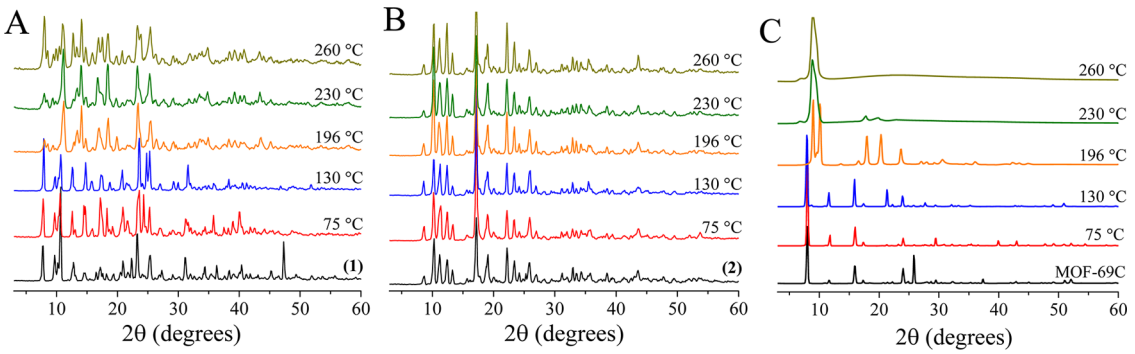

Figure 5. PXRD patterns after hourly evacuation at the designated temperatures of (A) (**1**); (B) (**2**); (C) MOF-69C.

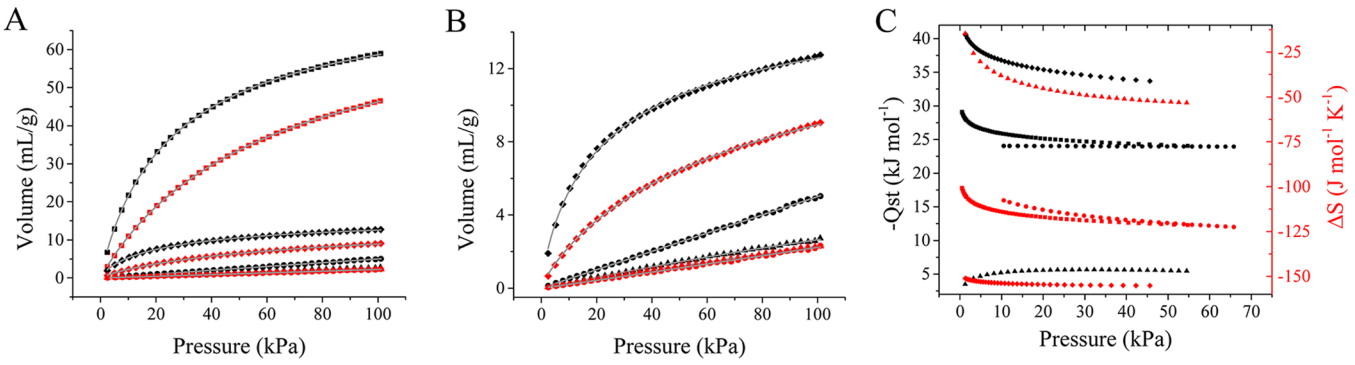

Figure 6. CO_2 isotherms at 273 K (black) and 296 K (red) with the Langmuir–Freundlich fit shown with solid line of (**1**) (squares), (**2**) (triangles), (**2**)-**MeOH** (diamonds), and MOF-69C (circles). Panel (A) shows all MOFs. Panel (B) shows zoom of lower adsorption. (C) Q_{st} (black) and ΔS (red) for (**1**) (squares), (**2**) (triangles), (**2**)-**MeOH** (diamonds), and MOF-69C (circles) as a function of pressure.

Table 2. Surface Area and Thermodynamic Parameters for CO_2 and N_2 Adsorption for (1), (2), (2)-MeOH, and MOF-69C

	determined from CO_2 sorption at 273 K					determined from N_2 sorption at 77 K	
MOF	BET (m^2/g)	langmuir (m^2/g)	Q_{st}[b] (kJ/mol)	Q_{st}^{0}[c] (kJ/mol)	K_F (Pa)	BET (m^2/g)	langmuir (m^2/g)
(**1**)	196	390	−29.1 ± 0.4	−27.7	45.9 ± 0.6	319	464
(**2**)	7	[a]	−3 ± 1	−2.7	1.7 ± 0.2	5	59
(**2**)-**MeOH**	41	74	−41 ± 4	−33.4	72 ± 2	39	59
MOF-69C	11	114	−24.1 ± 0.3	−17.6	5.72 (±0.01) × 10^{-2}	8	27

[a]Value could not be determined. [b]Determined from the Clausius–Clapeyron equation at the onset of adsorption. [c]Determined from the zero limit of the virial equation.

mL/g at ∼1 atm (Figures S14 and S15, Supporting Information) and surface areas of 41 and 74 m^2/g from BET and Langmuir analysis, respectively. The BET and Langmuir surface areas for all materials were calculated and are presented in Table 2.

The sorption properties of the MOFs were also investigated using N_2 at 77 K (Figure S16, Supporting Information). As was observed with CO_2, (**1**) exhibits a type-I isotherm and displays the greatest affinity for N_2. The BET and Langmuir surface areas for (**1**) were found to be 319 and 464 m^2/g, respectively (Table 2). MOF-69C and (**2**) exhibited a lower affinity for N_2

DOI: 10.1021/ic503047y
Inorg. Chem. 2015, 54, 4328−4336

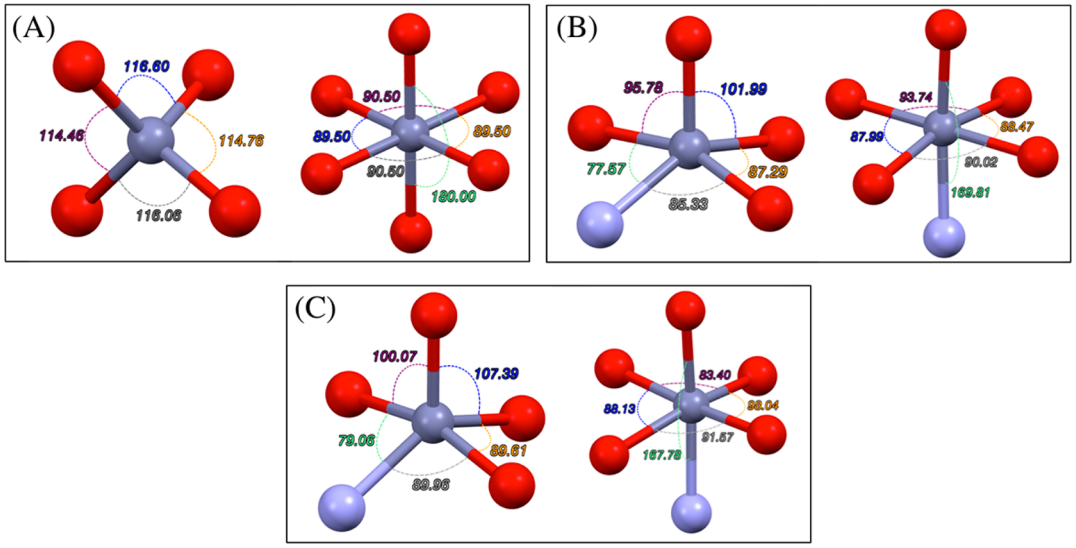

Figure 7. Metal coordination environments and selected bond angles for (A) MOF-69C (tetrahedral and octahedral); (B) (**1**) (distorted square pyramidal and octahedral); and (C) (**2**) (distorted square pyramidal and octahedral). The red circles represent oxygen, the light blue circles represent nitrogen, and the gray/blue circles represent zinc.

as compared to (**1**). The N_2 BET and Langmuir surface areas for (**2**) were found to be 5 and 59 m^2/g, respectively, and those for MOF-69C were found to be 8 and 27 m^2/g, respectively. The N_2 BET and Langmuir surface areas of (**2**)-**MeOH** were 39 and 59 m^2/g, respectively.

The thermodynamic properties of CO_2 adsorption were investigated by collecting isotherm data at 296 K in addition to the reported data at 273 K (Figure 6A,B). The volume adsorbed decreases with temperature for all compounds, confirming an exothermic nature to the adsorption process. A fit to the Langmuir–Freundlich isothermal equation (eq 1) was performed in order to determine the amount of gas adsorbed as a function of pressure[40−42]

$$\frac{Q}{Q_m} = \frac{K_F P^{(1/t)}}{1 + K_F P^{(1/t)}} \tag{1}$$

where Q is the moles of gas adsorbed, Q_m is the moles adsorbed at saturation, P is pressure, K_F is an affinity constant, and t is an index of heterogeneity ($0 < 1/t < 1$). Therefore, the Langmuir–Freundlich equation simplifies to the Langmuir equation when $t = 1$. The values of t required for adequate fits to the experimental data were very close to 1 for the as-synthesized MOFs, with a maximum deviation of 1.07 for (**1**). In fact, for CO_2 sorption on both MOF-69C and (**2**) at 296 K and MOF-69C at 273 K, the fits indicate a homogeneous binding environment with t equal to 1. However, (**2**)-**MeOH** gave a t value of 1.25 at 273 K, suggesting a heterogeneous binding environment,[41,42] which is consistent with CO_2 binding on the MOF/solvent surface rather than specifically within the pores of the MOF. Indeed, the lower value of Q_m for (**2**)-**MeOH** in comparison with (**1**) confirms that CO_2 does not penetrate the MOF pores. The sorption isotherms with the fits are shown in Figure 6, and the parameters are summarized in Table 2 and Table S5 (Supporting Information).

Application of the Clausius–Clapeyron equation (eq 2)[35] allows for the determination of the isosteric heats of adsorption, Q_{st}

$$\ln(P_i) = \frac{Q_{st}}{RT_i} + \frac{\Delta S}{R} \tag{2}$$

where P_i is the pressure for isotherm i, T_i is the temperature for isotherm i, R is the universal gas constant, and ΔS is entropy. The Langmuir–Freundlich equation was rearranged to solve for pressure and substituted into the Clausius–Clapeyron equation, which was used to determine the Q_{st} and ΔS for the MOFs (Figure 6C). It was observed that the adsorption enthalpy for (**1**) slightly decreases as the CO_2 pressure increases, remaining at a constant high negative value throughout the adsorption due to the favorable interactions between CO_2 and (**1**). The value of Q_{st} for (**1**) approaches −29.1 kJ/mol at low surface coverage. The adsorption enthalpies of (**2**) and MOF-69C at the onset of adsorption were found to be −3 and −24.1 kJ/mol, respectively, while the adsorption enthalpy for (**2**)-**MeOH** was −41 kJ/mol.

In order to further analyze the affinity of the framework for CO_2, the zero-coverage heat of adsorption (Q_{st}^0), which describes the strength of the binding sites within the material at the lowest pressures, can be determined by fitting the temperature-dependent isothermal data to a virial-type equation (eq 3)[7,43]

$$\ln P = \ln N + \frac{1}{T}\sum_{i=0}^{m} a_i N^i + \sum_{i=0}^{n} b_i N^i \tag{3}$$

where P is the pressure, N is the amount of CO_2 adsorbed, T is the temperature, m and n are the number of virial coefficients required for fitting, and a and b are virial coefficients. Contrary to the Langmuir equation, which goes to infinity at the zero pressure limit, the limit of the virial equation results in a numerical value used to estimate Q_{st}^0. In the equation, the parameters a_0 and b_0 are related to the Q_{st} and the Henry's Law constant (K_H), respectively. The enthalpies of adsorption can be estimated as a function of surface coverage (eq 4)[43]

$$Q_{st} = -R\left(\frac{d\ln P}{d\left(\frac{1}{T}\right)}\right)_N = -R\sum_{i=0}^{m} a_i N^i \tag{4}$$

DOI: 10.1021/ic503047y
Inorg. Chem. 2015, 54, 4328−4336

and the value of Q_{st}^0 determined by the limit of eq 4, as follows, eq 5:[7]

$$Q_{st}^{\ 0} = -R \lim_{N\to 0}\left(\sum_{i=0}^{m} a_i N^i\right) = -Ra_0 \tag{5}$$

Values of b_0 are also related to the physically meaningful quantity K_0, which is related to the Henry's Law adsorption constant, K_H, by eqs 6 and 7.[43]

$$K_H = K_0 \exp\left(\frac{q_0}{Rt}\right) \tag{6}$$

$$K_0 = \exp(-b_0) \tag{7}$$

Values of Q_{st}^0 for CO_2 adsorption on (**1**), (**2**), (**2**)-**MeOH**, and MOF69-C are presented in Table 2, and the corresponding fits are provided in Figures S17−S20 (Supporting Information).

The Q_{st}^0 values (from the onset of the Clausius−Clapeyron data and the virial equation) are consistent with a mechanism of CO_2 binding to (**1**) that involves the cationic Zn(II) metal sites present in the 3D structure. The calculated value of Q_{st}^0 (∼ −28 kJ/mol) agrees well with that observed for CPO-27-Zn (MOF-74-Zn, −30.5 kJ/mol) in which adsorption to coordinately unsaturated Zn(II) metal sites has been reported.[44] The larger Q_{st}^0 value for (**2**)-**MeOH** (∼33 kJ/mol) combined with the low coverage of CO_2 at equilibrium (Q_m) suggests physical interaction between CO_2 and a limited number of binding sites on the solvent-modified MOF surface, resulting in a larger adsorption enthalpy per binding site. Structurally, there are two main binding sites for CO_2 sorption in the materials presented: the metal nodes and the aromatic linkers. A key component to sorption at the metal nodes is the degree to which the CO_2 can enter the coordination sphere of the metal. To achieve coordinately unsaturated metal sites, CPO-27-M and other MOFs require activation, where a bound solvent molecule is removed through evacuation, solvent exchange followed by evacuation, or supercritical drying.[45] In contrast, both (**1**) and (**2**) exhibit Zn(II) metal nodes with a distorted 5-coordinate square pyramidal geometry as synthesized (Figure 7). Relatively minor structural rearrangements are required, if at all, to incorporate CO_2 into a sixth coordination site (attack from bottom, Figure 7). MOF-69C has a tetrahedral Zn(II) center (preferred geometry), and the structural rearrangement required to incorporate an additional ligand is much greater in comparison to that of (**1**) and (**2**). Therefore, it is likely that the mechanism of binding to MOF-69C is physisorption, consistent with that of MOF-5 (IRMOF-1) and UMCM-1. This agrees well with the calculated Q_{st}^0 for MOF-69C of ∼ −18 kJ/mol, whereas the measured Q_{st}^0 values for MOF-5 and UMCM-1 are −17 and −12 kJ/mol, respectively.[46,47] The sorption for (**2**) and (**2**)-**MeOH** is also likely a physisorption process on the surface of the MOF particles. While (**2**) exhibits binding sites that would be advantageous for CO_2 sorption, the void space is small (20.1 Å^3) and isolated, making gas permeation unfeasible. The DEF that is coordinated to the octahedral zinc would need to be removed to accommodate CO_2, and therefore, the potential for binding is not realized.

To quantify the selectivity of (**1**) for CO_2, isotherms for CO_2 and N_2 were recorded at the same temperature (296 K), allowing for a direct comparison of the amount of adsorbed gas. The selectivity of CO_2 over N_2 for (**1**) was calculated as the ratio of Henry's Law constants obtained as the pressure of the system goes to zero, which was estimated from the ratio of the initial slopes of the gas uptake (Figure S21, Supporting Information).[24] (**1**) preferentially adsorbs CO_2 over N_2 with a selectivity of 42, consistent with the thermodynamic analysis. This can be attributed to the fact that CO_2 has a larger polarizability than N_2, allowing the Lewis acidic metal node to bind to an oxygen atom of CO_2.[7,18] Additionally, CO_2 has a smaller kinetic diameter (3.30 Å) compared to N_2 (3.64 Å), which allows for easier diffusion of CO_2 within the MOF pores.[7,18] The kinetic effects are expected to contribute to a lesser degree than thermodynamics in this case.

The selectivity factor (S), which relates the molar ratio of adsorbed gases at the partial pressures of the gases within a mixture, is given by eq 8[7]

$$S = \frac{q_1/q_2}{p_1/p_2} \tag{8}$$

where q_i is the mass of adsorbed gas i at the relevant partial pressure, and p_i is the partial pressure of component i. For postcombustion CO_2 capture processes, the partial pressures of CO_2 and N_2 are 0.15 and 0.75, respectively.[7] It should be noted that the amount of gas adsorbed is determined from the single component sorption isotherm and does not take the competition of the gas molecules for adsorption sites into consideration. Therefore, the selectivity is not an accurate measure of how the MOF would behave in an actual mixed gas setting. S for (**1**) was found to be 14.

CONCLUSIONS

The solvothermal synthesis of two previously unreported MOFs was performed, and a thermodynamic study of their gas sorption properties was conducted. The MOFs contain Zn(II) metal sites in a distorted square pyramidal molecular geometry without the need of activation. These coordinately unsaturated metal nodes are ideal binding sites for the polarizable CO_2 molecule. The calculated isosteric heat of adsorption, Q_{st}, for (**1**) from both analysis by the Clausius−Clapeyron equation and the virial equation are consistent with this mechanism and other MOFs that exhibit Zn(II) metal binding sites (CPO-27-Zn). The microporous MOF, (**1**), displayed high selectivity for CO_2 over N_2 (42) as a result of both thermodynamic and, to a lesser extent, kinetic control.

ASSOCIATED CONTENT

Supporting Information

The crystallographic information, simulated PXRD patterns, the methods used to calculate adsorption enthalpy, and isotherm fits and parameters can be found in the Supporting Information. This material is available free of charge via the Internet at http://pubs.acs.org.

AUTHOR INFORMATION

Corresponding Author

*E-mail: ajmorris@vt.edu (A.J.M.).

Author Contributions

The manuscript was written through contributions of all authors, with the exception of Dr. Eva Marand, who is listed as an author on this manuscript posthumously.

Notes

The authors declare no competing financial interest.

DOI: 10.1021/ic503047y
Inorg. Chem. 2015, 54, 4328−4336

■ ACKNOWLEDGMENTS

The authors acknowledge the support of Virginia Tech's Institute for Critical Technologies and Applied Sciences for providing funding and the Sustainable Energy Lab for access to surface area and low-pressure characterization equipment.

■ REFERENCES

(1) Rosi, N. L.; Eddaoudi, M.; Kim, J.; O'Keeffe, M.; Yaghi, O. M. *CrystEngComm* **2002**, *4*, 401−404.
(2) Rowsell, J. L. C.; Yaghi, O. M. *Microporous Mesoporous Mater.* **2004**, *73*, 3−14.
(3) Eddaoudi, M.; Jaheon, K.; Rosi, N.; Vodak, D.; Wachter, J.; O'Keeffe, M.; Yaghi, O. M. *Science* **2002**, *295*, 469−472.
(4) Rosi, N. L.; Eckert, J.; Eddaoudi, M.; Vodak, D. T.; Kim, J.; O'Keeffe, M.; Yaghi, O. M. *Science* **2003**, *300*, 1127−1129.
(5) Collins, D. J.; Zhou, H.-C. *J. Mater. Chem.* **2007**, *17*, 3154−3160.
(6) Suh, M. P.; Park, H. J.; Prasad, T. K.; Lim, D.-W. *Chem. Rev.* **2011**, *112*, 782−835.
(7) Sumida, K.; Rogow, D. L.; Mason, J. A.; McDonald, T. M.; Bloch, E. D.; Herm, Z. R.; Bae, T.-H.; Long, J. R. *Chem. Rev.* **2012**, *112*, 724−781.
(8) Kaye, S. S.; Long, J. R. *J. Am. Chem. Soc.* **2005**, *127*, 6506−6507.
(9) Lee, J. Y.; Farha, O. K.; Roberts, J.; Scheidt, K. A.; Nguyen, S. B. T.; Hupp, J. T. *Chem. Soc. Rev.* **2009**, *38*, 1450−1459.
(10) Valvekens, P.; Vermoortele, F.; De Vos, D. *Catal. Sci. Technol.* **2013**, *3*, 1435−1445.
(11) Kreno, L. E.; Leong, K.; Farha, O. K.; Allendorf, M.; Van Duyne, R. P.; Hupp, J. T. *Chem. Rev.* **2012**, *112*, 1105−1125.
(12) Huxford, R. C.; Della Rocca, J.; Lin, W.-B. *Curr. Opin. Chem. Biol.* **2010**, *14*, 262−268.
(13) Zhuang, J.; Kuo, C.-H.; Chou, L.-Y.; Liu, D.-Y.; Weerapana, E.; Tsung, C.-K. *ACS Nano* **2014**, *8*, 2812−2819.
(14) Jeazet, H. B. T.; Staudt, C.; Janiak, C. *Chem. Commun.* **2012**, *48*, 2140−2142.
(15) David, O. C.; Gorri, D.; Urtiaga, A.; Ortiz, I. *J. Membr. Sci.* **2011**, *378*, 359−368.
(16) Schrock, R. R. *Proc. Nat. Acad. Sci.* **2006**, *103*, 17087−17087.
(17) Earth System Research Laboratory: http://www.esrl.noaa.gov/gmd/ccgg/trends/, 2014.
(18) Yang, R. T. *Adsorbents: Fundamentals and Applications*; John Wiley & Sons, Inc.: Hoboken, NJ, 2003.
(19) Wang, K.; Feng, D.; Liu, T.-F.; Su, J.; Yuan, S.; Chen, Y.-P.; Bosch, M.; Zou, X.; Zhou, H.-C. *J. Am. Chem. Soc.* **2014**, *136*, 13983−13986.
(20) Yang, S.; Sun, J.; Ramirez-Cuesta, A. J.; Callear, S. K.; DavidWilliam, I. F.; Anderson, D. P.; Newby, R.; Blake, A. J.; Parker, J. E.; Tang, C. C.; Schröder, M. *Nat. Chem.* **2012**, *4*, 887−894.
(21) D'Alessandro, D. M.; Smit, B.; Long, J. R. *Angew. Chem., Int. Ed.* **2010**, *49*, 6058−6082.
(22) McDonald, T. M.; D'Alessandro, D. M.; Krishna, R.; Long, J. R. *Chem. Sci.* **2011**, *2*, 2022−2028.
(23) Si, X.; Jiao, C.; Li, F.; Zhang, J.; Wang, S.; Liu, S.; Li, Z.; Sun, L.; Xu, F.; Gabelica, Z.; Schick, C. *Energy Environ. Sci.* **2011**, *4*, 4522−4527.
(24) An, J.; Geib, S. J.; Rosi, N. L. *J. Am. Chem. Soc.* **2010**, *132*, 38−39.
(25) Arstad, B.; Fjellvaag, H.; Kongshaug, K. O.; Swang, O.; Blom, R. *Adsorption* **2008**, *14*, 755−762.
(26) Cui, P.; Ma, Y.-G.; Li, H.-H.; Zhao, B.; Li, J.-R.; Cheng, P.; Balbuena, P. B.; Zhou, H.-C. *J. Am. Chem. Soc.* **2012**, *134*, 18892−18895.
(27) Yazaydin, A. O.; Snurr, R. Q.; Park, T.-H.; Koh, K.; Liu, J.; LeVan, M. D.; Benin, A. I.; Jakubczak, P.; Lanuza, M.; Galloway, D. B.; Low, J. J.; Willis, R. R. *J. Am. Chem. Soc.* **2009**, *131*, 18198−18199.
(28) Rosi, N. L.; Kim, J.; Eddaoudi, M.; Chen, B.; O'Keeffe, M.; Yaghi, O. M. *J. Am. Chem. Soc.* **2005**, *127*, 1504−1518.
(29) *CrysAlisPro Software System*; Agilent Technologies UK Ltd.: Oxford, UK, 2011.
(30) Sheldrick, G. M. *Acta Crystallogr.* **2008**, *A64*, 112−122.
(31) Dolomanov, O. V.; Bourhis, L. J.; Gildea, R. J.; Howard, J. A. K.; Puschmann, H. *J. Appl. Crystallogr.* **2009**, *42*, 339−341.
(32) Macrae, C. F. E.; P, R.; McCabe, P.; Pidcock, E.; Shields, G. P.; Taylor, R.; Towler, M.; van de Streek, J. *J. Appl. Crystallogr.* **2006**, *39*, 453−457.
(33) Brunauer, S.; Emmett, P. H.; Teller, E. *J. Am. Chem. Soc.* **1938**, *60*, 309−319.
(34) Langmuir, I. *J. Am. Chem. Soc.* **1932**, *54*, 2798−2832.
(35) Lowell, S.; Shields, J. E.; Thomas, M. A.; Thommes, M. *Characterization of Porous Solids and Powders: Surface Area, Pore Size and Density*; Kluwer Academic: Dordrecht, The Netherlands, 2004.
(36) Li, Z.-G.; Wang, G.-H.; Jia, H.-Q.; Hu, N.-H.; Xu, J.-W.; Batten, S. R. *CrystEngComm* **2008**, *10*, 983−985.
(37) Loiseau, T.; Muguerra, H.; Ferey, G.; Haouas, M.; Taulelle, F. *J. Solid State Chem.* **2005**, *178*, 621−628.
(38) Nugent, W. A.; Haymore, B. L. *Coord. Chem. Rev.* **1980**, *31*, 123−175.
(39) Hausdorf, S.; Wagler, J.; Mossig, R.; Mertens, F. O. R. L. *J. Phys. Chem. A* **2008**, *112*, 7567−7576.
(40) Yang, R. T. *Gas Separation By Adsorption Processes*; Butterworth: Boston, 1987.
(41) Jeppu, G. P.; Clement, T. P. *J. Contam. Hydrol.* **2012**, *129*−*130*, 46−53.
(42) Turiel, E.; Perez-Conde, C.; Martin-Esteban, A. *Analyst (Cambridge, U. K.)* **2003**, *128*, 137−141.
(43) Czepirski, L.; Jagiello, J. *Chem. Eng. Sci.* **1989**, *44*, 797−801.
(44) Valenzano, L.; Civalleri, B.; Sillar, K.; Sauer, J. *J. Phys. Chem. C* **2011**, *115*, 21777−21784.
(45) Mondloch, J. E.; Karagiaridi, O.; Farha, O. K.; Hupp, J. T. *CrystEngComm* **2013**, *15*, 9258−9264.
(46) Choi, J.-S.; Son, W.-J.; Kim, J.; Ahn, W.-S. *Microporous Mesoporous Mater.* **2008**, *116*, 727−731.
(47) Mu, B.; Schoenecker, P. M.; Walton, K. S. *J. Phys. Chem. C* **2010**, *114*, 6464−6471.

DOI: 10.1021/ic503047y
Inorg. Chem. 2015, 54, 4328−4336